

Local Crystal Structure of Antiferroelectric $\text{Bi}_2\text{Mn}_{4/3}\text{Ni}_{2/3}\text{O}_6$ in Commensurate and Incommensurate Phases Described by Pair Distribution Function (PDF) and Reverse Monte Carlo (RMC) Modeling

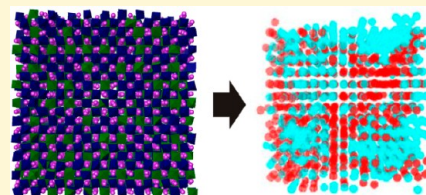
Robert J. Szczecinski,[†] Samantha Y. Chong,[†] Philip A. Chater,[†] Helen Hughes,[†] Matthew G. Tucker,[‡] John B. Claridge,^{*,†} and Matthew J. Rosseinsky[†]

[†]Department of Chemistry, University of Liverpool, Liverpool L69 7ZD, U.K.

[‡]ISIS Facility, Rutherford Appleton Laboratory, Harwell, Didcot OX11 0DE, U.K.

S Supporting Information

ABSTRACT: The functional properties of materials can arise from local structural features that are not well determined or described by crystallographic methods based on long-range average structural models. The room temperature (RT) structure of the Bi perovskite $\text{Bi}_2\text{Mn}_{4/3}\text{Ni}_{2/3}\text{O}_6$ has previously been modeled as a locally polar structure where polarization is suppressed by a long-range incommensurate antiferroelectric modulation. In this study we investigate the short-range local structure of $\text{Bi}_2\text{Mn}_{4/3}\text{Ni}_{2/3}\text{O}_6$, determined through reverse Monte Carlo (RMC) modeling of neutron total scattering data, and compare the results with the long-range incommensurate structure description. While the incommensurate structure has equivalent B site environments for Mn and Ni, the local structure displays a significantly Jahn–Teller distorted environment for Mn^{3+} . The local structure displays the rock-salt-type Mn/Ni ordering of the related $\text{Bi}_2\text{MnNiO}_6$ high pressure phase, as opposed to Mn/Ni clustering observed in the long-range average incommensurate model. RMC modeling reveals short-range ferroelectric correlations between Bi^{3+} cations, giving rise to polar regions that are quantified for the first time as existing within a distance of approximately 12 Å. These local correlations persist in the commensurate high temperature (HT) phase, where the long-range average structure is nonpolar. The local structure thus provides information about cation ordering and B site structural flexibility that may stabilize Bi^{3+} on the A site of the perovskite structure and reveals the extent of the local polar regions created by this cation.



INTRODUCTION

The crystal structures of materials are traditionally investigated by the long-range phenomenon of Bragg diffraction and described by unit cells that represent the average structure. Atoms in the structure are described in terms of positions and thermal vibrations that are time averaged over all unit cells. The structure of a functional material controls its properties. In cases where the composition necessarily imposes disorder on the structure, it is challenging to develop a complete picture of that structure over the different length scales on which this disorder can manifest itself. This has become clear in recent investigations of functional electroceramics such as the relaxor ferroelectric perovskite PMN-PT, where the disorder between Mg and Nb is not resolved crystallographically in the average structure but clearly contributes to dynamic and static polarization phenomena as revealed by single crystal diffuse scattering measurements.¹ Similarly $\text{Pb}(\text{Zr,Ti})\text{O}_3$ (PZT), which has applications as piezo sensors, actuators, sonars, and transducers,² displays structural heterogeneity that is critical for the formation of the morphotropic phase boundary that produces its properties but to which Bragg diffraction is surprisingly insensitive.³ Perovskites with Bi^{3+} cations on the A

site are potential alternatives to these Pb^{2+} -based functional materials due to the $6s^2$ lone pair that is common to both cations. The hybridization between Bi 6s and oxygen 2p states stabilizes the off-center displacement of Bi^{3+} cations and produces ferroelectricity. Apart from the well-studied antiferromagnetic ferroelectric BiFeO_3 ,^{4,5} most Bi-based perovskites require high pressure (HP) synthesis because of the difficulty of accommodating the small Bi^{3+} cation on the 12-coordinate A site,^{6–12} e.g., BiMnO_3 and $\text{Bi}_2\text{MnNiO}_6$. It is thus of interest to expand the number of materials with Bi^{3+} on the perovskite A site that are accessible under ambient pressure synthesis conditions.^{2,4,13–15} This can be achieved by increasing the number of cations on the B site and thus the ability of this site to adapt to the coordination requirements of Bi^{3+} , as in $\text{BiTi}_{3/8}\text{Fe}_{2/8}\text{Mg}_{3/8}\text{O}_3$ ¹⁴ or $\text{Bi}_2\text{Mn}_{4/3}\text{Ni}_{2/3}\text{O}_6$ (BMN), the subject of the present study, which has two different B site cations with three oxidation states (Mn^{4+} , Mn^{3+} , and Ni^{2+}).¹³ As the multiple B site cations are not completely ordered in the

Received: November 20, 2013

Revised: February 20, 2014

Published: February 21, 2014

average structure, an understanding of the chemical factors contributing to the unexpected stability of these systems requires local structural information. Given the importance of short-range structural motifs in controlling the functional behavior of lead-based electroceramics, this local structure information is also needed to understand the properties of A site Bi^{3+} perovskites.

BMN is incommensurate at room temperature (RT), as evidenced by the presence of satellite reflections in the powder diffraction pattern, which are produced by modulations that occur beyond the length scale of the incommensurate subcell. These modulations can be in the form of positional or occupational perturbations to the atoms in the subcell and can result in a more diverse range of local environments than a traditional unit cell description. Incommensurate structures are frequently visualized using an approximant incommensurate supercell, which is a multiple of the subcell where the period of the modulations is near integer values. The incommensurate structure of BMN has been determined in the centrosymmetric space group ($Ibmm(\alpha 00, 0-\beta 0)mm.ss$).¹⁶ The incommensurate subcell consists of a $\sqrt{2}a_p \times 2a_p \times \sqrt{2}a_p$ expansion of an orthorhombic perovskite structure (a_p denotes cubic perovskite subcell lattice parameter, ~ 3.8 Å) where Bi displacements along the $\langle 100 \rangle$ direction cancel to give a nonpolar subcell structure. The subcell is modulated by positional and occupational modulations of the atoms in higher dimensional space along the $\langle 100 \rangle$ and $\langle 010 \rangle$ directions, which correspond to ideal cubic perovskite directions $\langle 1\bar{1}0 \rangle_p$ and $\langle 001 \rangle_p$, respectively (Figure 1). For consistency, throughout this work we will relate all crystallographic directions back to those of the ideal cubic perovskite unit cell and denote these as $\langle hkl \rangle_p$. The modulation in the BMN structure is described by two modulation vectors, $q_1 = \alpha a^*$ ($\alpha = 0.4930(3)$) and $q_2 = \beta b^*$ ($\beta = -0.4210(7)$), which define a fourth and fifth dimension and occur along $\langle 1\bar{1}0 \rangle_p$ and $\langle 001 \rangle_p$ directions, respectively. Displacive modulations of the A site give rise to a wide range of Bi environments and induce locally polar regions along $\langle 1\bar{1}0 \rangle_p$ from the nonpolar subcell which cancel over longer length scales to produce long-range antiferroelectric displacements; the result is that the approximant incommensurate supercell ($71\sqrt{2}a_p \times 38a_p \times \sqrt{2}a_p$) has almost no polarization ($2 \mu\text{C cm}^{-2}$).¹⁶ The short-range structural behavior along the locally polar $\langle 1\bar{1}0 \rangle_p$ direction is therefore of great interest, as this controls the key physical property. A phase transition is observed upon heating at ~ 200 °C where the long-range incommensurate modulations are lost. The long-range average high temperature (HT, measured here at 300 °C) structure is commensurate and antiferrodistortive (GdFeO₃ structure, space group $Pcmm$ in the orthorhombic setting consistent with the other structures discussed here, unit cell size $\sqrt{2}a_p \times 2a_p \times \sqrt{2}a_p$) and has a single regular A site environment.

Both the incommensurate (RT) and commensurate (HT) structures of BMN described above are derived from diffraction phenomena and represent a long-range average of the true local structure that may not adequately describe the diversity of short-range structural features that can be responsible for the observed chemical stability and physical properties. In order to determine the true local structure of a material, one has to reduce the reliance on Bragg diffraction and make use of diffuse scattering that lies in the background of a diffraction pattern. The simultaneous analysis of Bragg and diffuse scattering data is known as total scattering analysis, described in detail in Supporting Information section S1. We employ the reverse

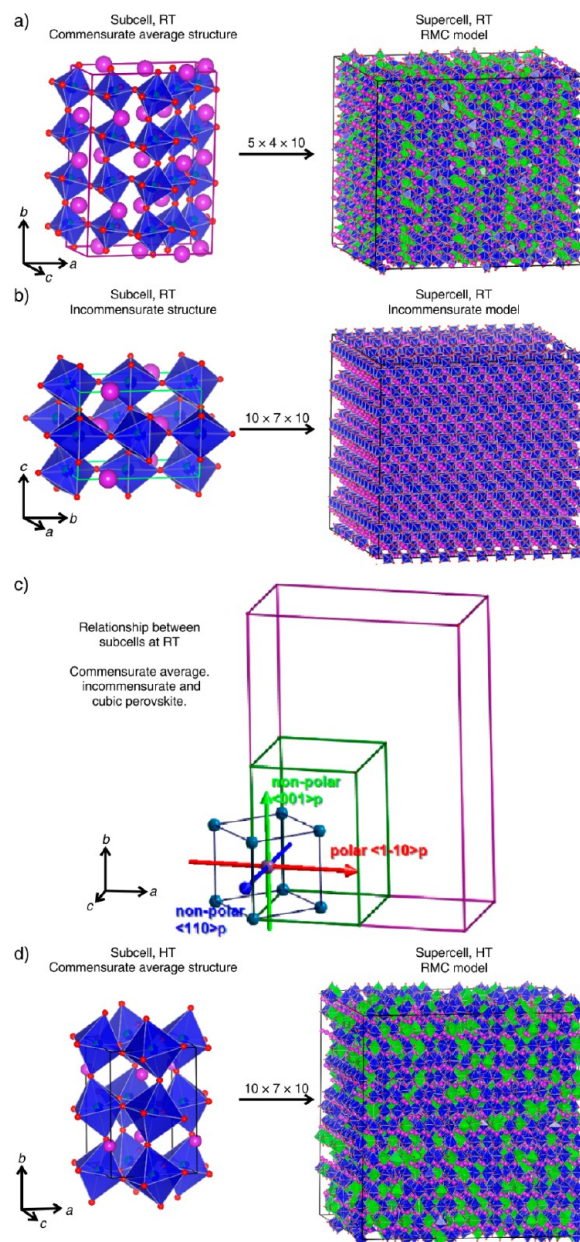


Figure 1. (a) Subcell of the commensurate average crystallographic structure $P2_1mn$ at RT and an RMC supercell obtained by multiplicity of $5 \times 4 \times 10$ subcells. (b) Subcell of the incommensurate structure $Ibmm(\alpha 00, 0-\beta 0)mm.ss$ and a supercell of comparable size to the RMC supercell. (c) Representation of $\text{Bi}_2(\text{Mn}_{4/3}\text{Ni}_{2/3})\text{O}_6$ (Bi shown as pink-purple spheres, B cation sites as light blue spheres) within pseudo-cubic (dark blue box), commensurate average $P2_1mn$ (purple box), and incommensurate orthorhombic $Ibmm$ (green box) unit cells with corresponding pseudo-cubic directions polar $\langle 1\bar{1}0 \rangle_p$ and nonpolar $\langle 110 \rangle_p$ and $\langle 001 \rangle_p$. (d) Subcell of the commensurate average crystallographic structure $Pcmm$ at HT and the RMC supercell obtained by multiplicity $10 \times 7 \times 10$ subcells. All three structures, $P2_1mn$, $Ibmm$, and $Pcmm$, and their supercells have the same unit cell axis settings.

Monte Carlo (RMC) optimization of the positions of atoms within a large supercell of the average structure to fit the conventional Bragg scattering together with the pair distribution function (PDF) which describes the probability of two atoms being separated by a distance r .¹⁷ PDF studies have established the local structures of Pb-based perovskite materials,

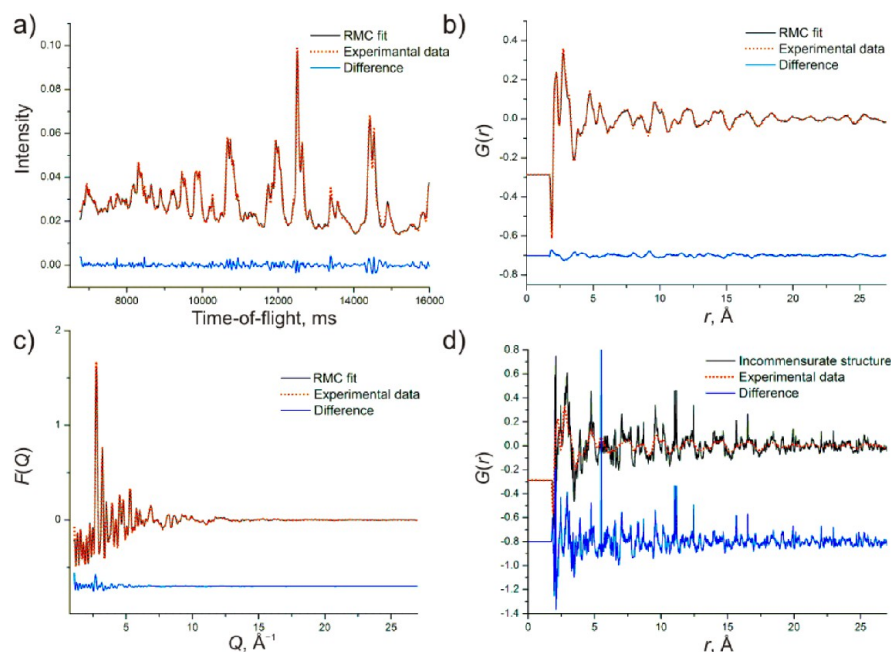


Figure 2. Comparison between measured and calculated functions of one of the RMC models of the local structure of $\text{Bi}_2\text{Mn}_{4/3}\text{Ni}_{2/3}\text{O}_6$ at RT: (a) Bragg profile data; (b) total correlation function $G(r)$; (c) total scattering structure factor $F(Q)$. The total correlation function, $G(r)$, of the incommensurate structure is compared to the observed data in (d).

where condensation of static polar nanoregions (PNR) at high temperature has been identified in relaxor ferroelectrics such as $\text{Pb}(\text{Mg}_{1/3}\text{Ta}_{2/3})\text{O}_3$.^{18–20} The investigation of lead-free ferroelectric materials revealed significant differences between the average and local structures of importance in understanding the ferroelectric properties.^{21–23} In contrast to the Pb systems, the local structures and short-range correlations of pure Bi A site perovskites have not been extensively studied. In BiMnO_3 , PDF analysis showed the existence of ferroelectric domains larger than 100 Å.²⁴ In $\text{BiTi}_{3/8}\text{Fe}_{2/8}\text{Mg}_{3/8}\text{O}_3$, the local structure revealed local correlations of Bi displacements producing monoclinic domains that could not be deduced from the average rhombohedral structure. PDF analysis also contributed to the understanding of the stability of pure Bi^{3+} A site perovskite materials by revealing the local bonding environments at the three B cations, which are all disordered onto one site in the average structure.²⁵

BMN is more complex than electroceramics previously studied by PDF methods, as it has an incommensurate structure at room temperature. PDF studies on incommensurate structures as a class are rare; PDF analysis of incommensurate charge-density waves in CeTe_2 revealed significantly larger amplitudes of local atomic distortions in the Te coordination environment than in the crystallographic structure.²⁶ In order to resolve the local structure and local polar nature of BMN in both the incommensurate RT and commensurate HT phases, the RMC method was applied to neutron total scattering data and the resulting models were analyzed to yield local bonding information and atomic correlations. The emerging structural picture is distinct from any reported in lead-based materials and demonstrates the need to combine both average and local structures to understand the chemical control of polar behavior in Bi-based electroceramics.

EXPERIMENTAL METHOD AND DATA ANALYSIS

The samples were prepared by a standard ceramic method described by Claridge et al.¹⁶ Samples (5 g) were contained in 8 mm diameter vanadium cans. Neutron total scattering data were collected at general materials diffractometer (GEM) at the ISIS pulsed spallation neutron source.²⁷ RT and HT data at 300 °C were collected for 920 and 1135 $\mu\text{A h}$, respectively, over the same scattering vector range, $0.3 \leq Q \leq 50 \text{ \AA}^{-1}$. The high scattering vector accessible on GEM produces good real-space resolution in the PDF data ($\Delta r \approx (2\pi/Q_{\text{max}})$; so for $Q_{\text{max}} = 50 \text{ \AA}^{-1}$, $\Delta r \approx 0.13 \text{ \AA}$). All of the supercells used in the RMC analysis were approximate cubes containing 16 000 atoms. The starting model for the RT structure was based on the commensurate $2\sqrt{2}a_p \times 4a_p \times \sqrt{2}a_p$ subcell in the polar orthorhombic space group $P2_1mn$, previously identified as the best commensurate approximation to the incommensurate structure.¹⁶ The GdFeO_3 -related structure was used as the starting model for the HT analysis. At the start of the RMC refinement, atom types were assigned randomly to B sites consistent with the fractional occupancies of the parent models, i.e., 2:1 Mn/Ni for the RT and HT models. Models of the incommensurate structure of the same size as the RMC models were derived by taking appropriate sized sections of an approximate supercell derived from the incommensurate structure; atom types were assigned randomly to B sites in a manner consistent with the occupational probability from the modulated model. The relationships between these models can be found in Figure 1, and the generation of the models is described in more detail in Supporting Information section S2. Because of the underdetermined nature of the PDF refinements, it is generally necessary to apply some chemical constraints to the model in order to obtain meaningful results; here we used bond valence sum (BVS) constraints on the metal–oxygen distances for RT and HT models and an interatomic potential for Ni–O octahedra in the RT model. For the RT structure, the RMC refinement was started with only swapping of B site atoms allowed, followed by a second refinement step in which the B site atom swapping was replaced by atomic translation moves. During the RMC refinement of the HT structure, simultaneous atom translations and swapping of B site cations were performed. RMC runs with and without data (referred to as “data-free refinements” in what follows) were performed in order to confirm that these did not prejudice the overall result, as set out in more detail in Supporting Information section S2.

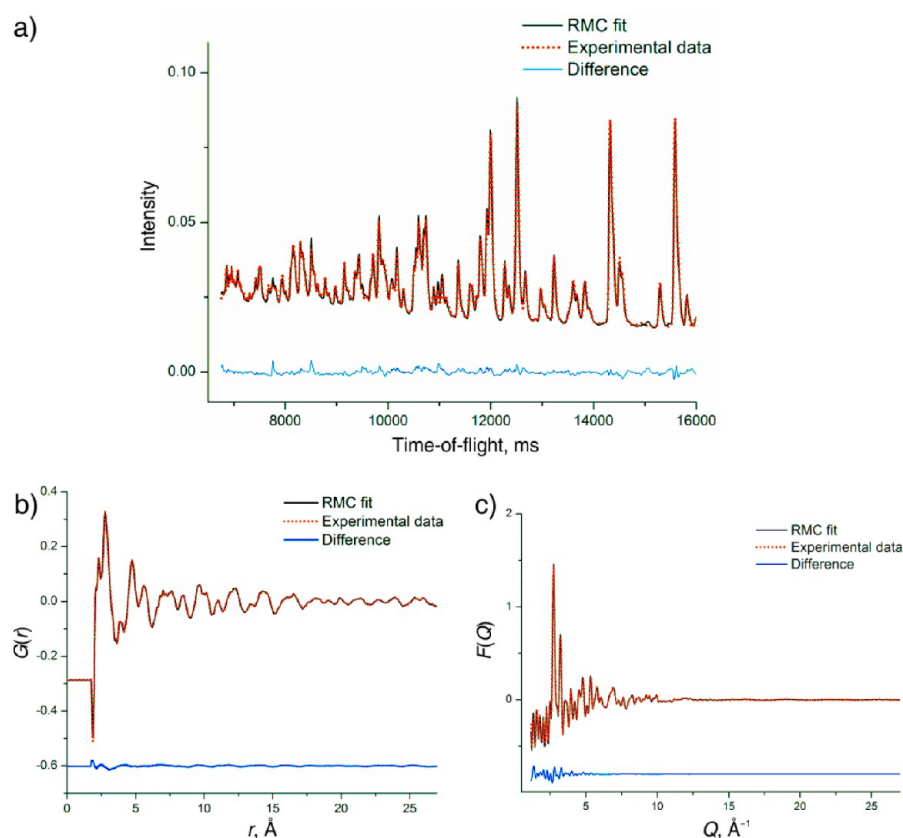


Figure 3. Comparison between measured and calculated functions of one of the RMC models of the local structure of $\text{Bi}_2\text{Mn}_{4/3}\text{Ni}_{2/3}\text{O}_6$ at HT: (a) Bragg profile data; (b) total correlation function $G(r)$; (c) total scattering structure factor $F(Q)$.

Table 1. Comparison of Bi–O Bond Distances from the Pair Distribution Function Analysis of $\text{Bi}_2\text{Mn}_{4/3}\text{Ni}_{2/3}\text{O}_6$ Calculated for Incommensurate (RT) and Commensurate (HT) Phases for the Average Crystallographic Structure and the Local Structure (from RMC Refinement)^a

Bi–O Bond Length, Å			
RT		HT	
average incommensurate model	RMC local structure	average commensurate structure	RMC local structure
2.241(13)	2.252(5)	2.337	2.307(3)
2.43(3)	2.685(2)	2.442 (×2)	2.611(2)
2.99(3)	3.151(9)	2.448	3.234(9)
(1.29:4.26:6.45) ^b	(3.84:4.8:3.36) ^b	2.659 (×2)	(3.84:2.89:5.26) ^b
		2.697 (×2)	
		3.171	
		3.217	
		3.383 (×2)	

^aDistances for the average incommensurate model and the RMC local structure were obtained by fitting Gaussian functions to the observed partial pair distribution functions (Figure 3), while distances listed for the commensurate (HT) phase are the 12 nearest Bi–O distances from the average crystallographic model. ^bApproximate ratio of bond distances (summed to 12 oxygen coordinate system) obtained from the integrated areas of peaks in $g_{\text{Bi–O}}(r)$ for the average incommensurate model and the RMC local structure model in the RT and HT structures.

RESULTS

RMC refinement of the RT and HT starting configurations (described above) gave very good fits to the observed Bragg profile, total scattering structure factor $F(Q)$, and the PDF $G(r)$ (Figures 2 and 3, respectively). The PDF of the RMC-refined local structure at RT was compared with the PDF calculated from the supercells of the incommensurate average structure generated using Jana²⁸ in order to highlight the differences in description of the bonding between the present local structure refinement and the reported average incommensurate structure. The fit of the incommensurate structure to the observed $G(r)$

data is shown in Figure 2d; it is clear that the incommensurate average structure does not adequately describe the observed local structure in the $G(r)$ data. The extra information derived from the local structure description in several key aspects of structural understanding is discussed below. Average bond distances for both the local structure and the incommensurate average structure were estimated by fitting Gaussian functions to the observed partial pair distribution functions, $g_{ij}(r)$, which represents distribution of bond distances for every pair of atom types, as described in eq 4 (Supporting Information section S1).

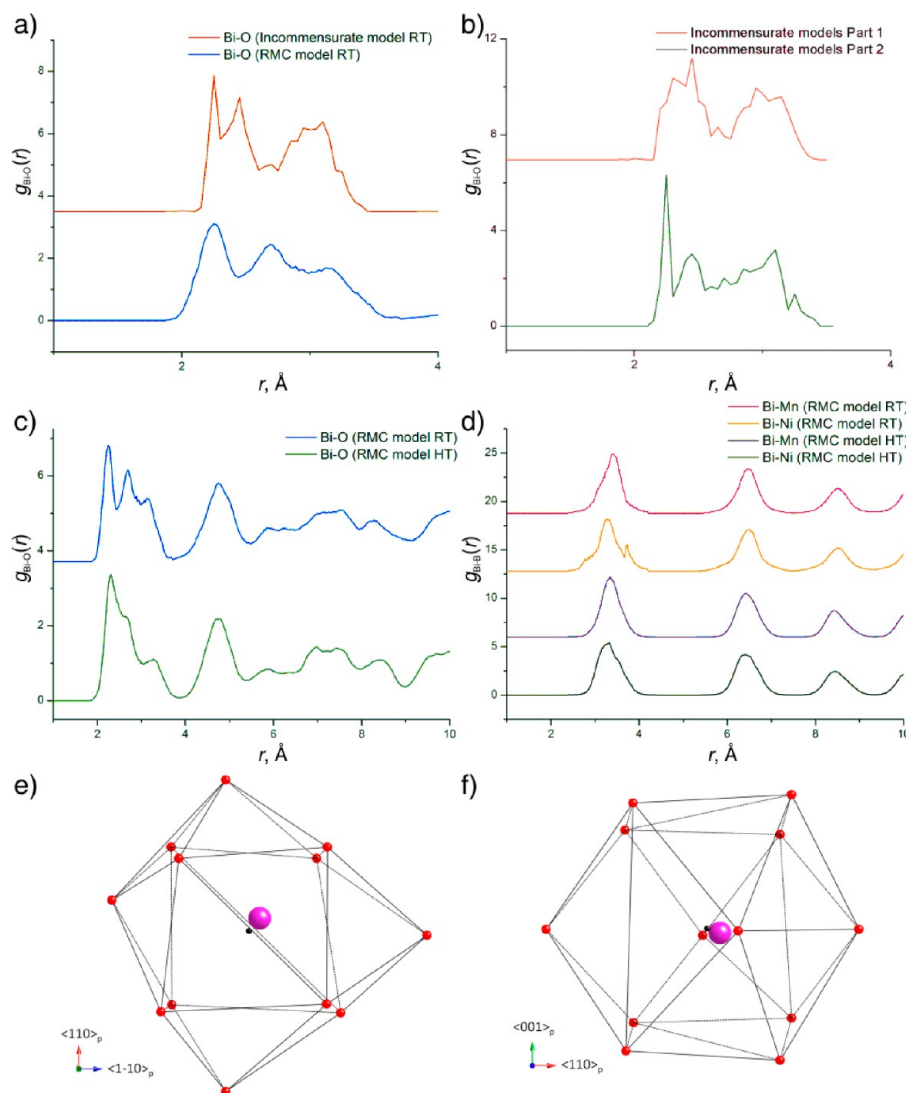


Figure 4. Partial pair correlation functions: (a) $g_{Bi-O}(r)$ derived from the RMC local structure and average incommensurate model at RT; (b) two general different shapes of $g_{Bi-O}(r)$ derived from different incommensurate models at RT; (c, d) comparison of (c) $g_{Bi-O}(r)$ and (d) $g_{Bi-B}(r)$, respectively, for the RMC local structure at RT and HT. Representation of the local structure of the most common Bi cation displacement (purple sphere) from the oxygen centroid (indicated as a black sphere), shown relative to the oxygen positions from the crystallographic average structure (red spheres) viewed down (e) $\langle 110 \rangle_p$ and (f) $\langle 001 \rangle_p$. The results are based on the mode value of the displacements in the RMC models with the most significant displacement of Bi^{3+} of 0.283 Å along nonpolar $\langle 110 \rangle_p$ and smaller displacements of 0.099 and 0.052 Å along polar $\langle 110 \rangle_p$ and nonpolar $\langle 001 \rangle_p$ directions, respectively.

Bi–O Environments. Initial comparison of the $g_{Bi-O}(r)$ between the average incommensurate model and the RMC local structure showed similar Bi–O distances for both models (Table 1). The $Bi^{3+}-O^{2-}$ distances at RT (Figure 4a) in both the RMC local structure and the average incommensurate model produce three main groups of bond distances (2.252(5), 2.685(2), and 3.151(9) Å for the RMC local structure and 2.241(13), 2.43(3), and 2.99(3) Å for the average incommensurate structure). These peaks are entirely absent in the data-free RMC refinements and so are a result of the experimental data rather than any applied restraints. The area of the first strong peak in the RMC local structure (Table 1) indicates that Bi atoms move toward the four nearest oxide neighbors to create short Bi–O distances of 2.252(5) Å. Comparison of the groups of Bi–O bond distances between the refined RMC local structure and the models calculated from the average incommensurate structure indicates a broader range of Bi–O bond distances for the RMC models. The relatively

broad Bi–O distributions in the RMC local structure are attributed to thermal motion, whereas the average incommensurate model includes thermal motion as time averaged thermal ellipsoids around an average atomic position. However, closer inspection of $g_{Bi-O}(r)$ of the 10 individual incommensurate models studied shows two different shapes of distribution (Figure 4b); half of the models showed a sharp first peak, and the other half showed a smoother distribution that was fitted to two Gaussian peaks. The presence of two types of $g_{Bi-O}(r)$ is a result of the modulations used in the incommensurate structure. The smoother distribution, defined as incommensurate models part 1 (Figure 4b top), gives Bi–O bond distances of 2.386(4) and 3.007(3) Å with a ratio of 5.82:6.18 for the 12 nearest neighbors. This is consistent with antiparallel displacement of Bi cations along $\langle 110 \rangle_p$ which would ideally give rise to five short, two medium, and five long Bi–O bonds; we do not observe the two medium bonds as distinct peaks because they will lie beneath the two main observed peaks in $g_{Bi-O}(r)$. On

the other hand, the sharp peak in the second type of distribution, defined as incommensurate models part 2 (Figure 4b bottom), is likely due to maxima in the modulations that add constructively to produce a narrow distribution of short Bi–O bonds which is not representative of the true local structure, which is observed by RMC. The application of incommensurate modulations to atomic positions produces a discontinuous distribution of Bi–O distances due to local minima and maxima in the modulated displacements. The average incommensurate model $g_{\text{Bi-O}}(r)$ distribution (Figure 4a) contains features from both types of distribution (part 1 and part 2) and as such makes determining average bond lengths from this data misleading. A representation of the most common Bi local environment determined through RMC modeling is shown in Figure 4e and Figure 4f. The Bi cation is clearly displaced from the center of the coordinating oxygen atoms, with the displacement predominantly along $(110)_p$.

The local structure at HT is consistent with the average commensurate crystallographic structure, with a comparable range of Bi–O distances (Table 1). The RMC $g_{\text{Bi-O}}(r)$ is significantly broader and less well separated at HT than at RT (Figure 4c), as expected because of increased thermal motion at HT. The shortest bond length increases from 2.252(5) Å at RT to 2.307(3) Å at HT, and the longest bond length increases from 3.151(9) Å at RT to 3.234(9) Å at HT. The intermediate bond length decreases slightly from 2.685(2) Å at RT to 2.611(2) Å at HT.

A Site–B Site Separations. The Bi^{3+} cations are expected to be sensitive to the local B site occupancy. Inspection of the distribution of bond distances between Bi and B site cations (Figure 4d) shows that Bi^{3+} atoms prefer to move toward Ni^{2+} neighbors and away from manganese cations, which is in agreement with expectations based on electrostatics, although correlations between these displacements are weak and short-range (see section S3 and Figure S1 in Supporting Information). These differences are shown by the respective distances: Bi–Mn 3.412(1) Å and Bi–Ni 3.273(1) Å in the RT structure. Furthermore the trend of bond distances between Bi and B site cations is preserved at HT where Bi–Mn and Bi–Ni distances of 3.358(14) and 3.224(12) Å, respectively, are observed (Table S1 in Supporting Information). Data-free refinements revealed a similar trend but to a much reduced extent (RT Bi–Mn 3.364(2) Å, Bi–Ni 3.307(2) Å; HT Bi–Mn 3.352(5) Å, Bi–Ni 3.316(7) Å), indicating that while this trend may in part be a result of the BVS restraint, the result is dominated by the observed data.

Mn–O and Ni–O Environments. The local bonding at the Mn and Ni sites is revealed by the partial pair distributions, $g_{\text{B-O}}(r)$ (Figure 5), which were analyzed by fitting Gaussian functions to the observed distributions. The average incommensurate model, where three B cations are disordered onto one site, has a relatively narrow distribution of B–O bond distances; the RT local structure shows a significantly broader distribution for both B sites. The interatomic potential applied to Ni–O pairs in the RT RMC refinement yields a symmetric $g_{\text{Ni-O}}(r)$ and an average bond distance of 2.075(1) Å, which is in agreement with those reported for $\text{Bi}_{0.5}^{3+}\text{Bi}_{0.5}^{5+}\text{Ni}^{2+}\text{O}_3$.^{6,12} The $g_{\text{Mn-O}}(r)$ in contrast presents a more complex asymmetric distribution. The Mn BVS distribution of the RT RMC local structure models shows a unimodal Gaussian distribution around an average oxidation state of +3.43, indicating that in the local structure models the Mn adopts an oxygen coordination environment between that expected for Mn^{4+}

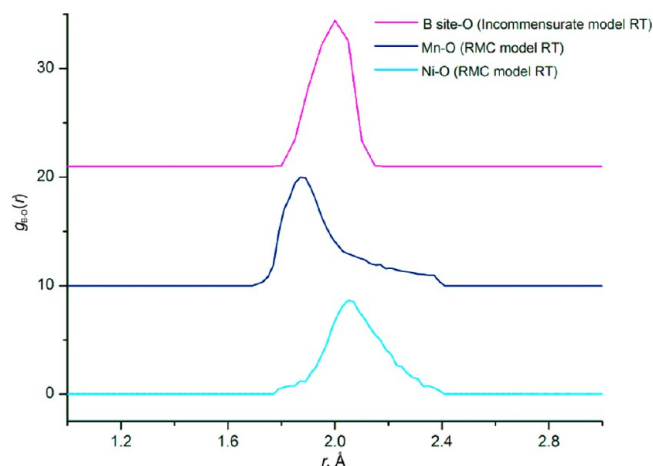


Figure 5. Comparison of the partial pair correlation functions $g_{\text{B-O}}(r)$ between the average incommensurate model and the RMC local structure at RT. The local structure enables the differentiation between the different B site cations and reveals a broader distribution of bond lengths than for the average incommensurate model.

and Mn^{3+} . However, the ideal Mn–O bond lengths for six-coordinate Mn^{4+} and Mn^{3+} from BVS calculations vary only slightly (1.90 and 2.01 Å, respectively),²⁹ and so differences in charge alone cannot account for the large range of observed bond lengths. Instead, we attribute the broad asymmetric $g_{\text{Mn-O}}(r)$ distribution to the presence of both undistorted Mn^{4+} and Jahn–Teller (J–T) distorted Mn^{3+} . Mn^{4+} typically displays six bond distances of approximately 1.9 Å, while Mn^{3+} with J–T distortions adopts a broad variety of bond distances. The most common J–T phenomena produce lattice distortions giving four short (~ 1.92 – 1.96 Å) and two long bond distances (~ 2.11 – 2.16 Å), herein referred to as 4:2 J–T, as observed in LaMnO_3 ³⁰ or A site doped $\text{La}_{1-x}\text{Ca}_x\text{MnO}_3$ ³¹ and $\text{La}_{1-x}\text{Sr}_x\text{MnO}_3$.³² However, in the bismuth-based perovskite $\text{Bi}_{1-x}\text{Ca}_x\text{MnO}_3$ ³³ there is a different pattern of two short bonds (~ 1.9 Å), two long equatorial bonds (~ 2.1 Å), and two medium apical bonds (~ 1.95 Å), herein referred to as 2:2:2 J–T. The same J–T feature is also observable in BiMnO_3 ,⁵ where the bond length distribution is broader (~ 1.8 , ~ 2.0 , and ~ 2.2 Å). In order to determine which type of J–T distortion is most consistent with our data, the $g_{\text{Mn-O}}(r)$ was fitted with two and three Gaussian peaks. We would expect to observe a single Gaussian contribution from undistorted Mn^{4+} , and a range of bond distances from Mn^{3+} (some of which may overlap with Mn^{4+} –O distances) corresponding to one of the J–T distortion types (4:2 J–T or 2:2:2 J–T). Three Gaussian functions gave a much better fit to the Mn–O distribution than two Gaussians and gave average bond lengths of 1.859(9), 1.946(11), and 2.146(57) Å (Table 2). The ratio of integrated areas for these different bond lengths normalized to 12 oxygen nearest neighbors (6 for Mn^{4+} and 6 for Mn^{3+}) is approximately 6:3:3. The identical ratio for two medium and long bond lengths and the better fit of three Gaussian functions than two indicate that the Mn–O bond distances observed in the local structure are more consistent with the 2:2:2 J–T distortions observed for both BiMnO_3 and $\text{Bi}_{1-x}\text{Ca}_x\text{MnO}_3$. The larger number of short than medium or long bonds (ratio of 6:3:3 respectively) may be attributed to the very comparable bond distances for both regular Mn^{4+} and the shortest bond distance in J–T distorted Mn^{3+} cations. However, the integrated area for the different bond lengths is approximately 6:3:3, as opposed to

Table 2. Comparison of B Site–O Bond Distances for the Average Incommensurate Model and the RMC Local Structure at RT

average incommensurate model	B–O Bond Length, Å	
	RMC local structure	
1.99(3)	Mn–O	Ni–O
	1.859(9)	2.075(1)
	1.946(11)	
	2.146(57)	
	(6:3:3) ^a	

^aApproximate ratio of bond distances (summed to 12, rather than the coordination number of 6, because of the presence of both Mn³⁺ and Mn⁴⁺ cations) obtained from the integrated areas of peaks in $g_{B-O}(r)$ for the RMC local structure models at RT.

8:2:2 expected for an idealized case of a regular Mn⁴⁺ and a 2:2:2 J–T Mn³⁺, indicating that the observed Mn–O coordination environment is more complex.

Consistent with this, the average structure of the related high pressure phase Bi₂NiMnO₆, which is nominally Mn⁴⁺ and therefore free from J–T distortion, also displays a range of Mn–O distances (from 1.83(7) to 2.10(5) Å) that is relatively wide when compared to the narrow distributions of Ni–O bonds in the same structure (1.97(6)–2.08(5) Å).⁹ J–T distortions in Bi₂Mn_{4/3}Ni_{2/3}O₆ due to the presence of Mn³⁺ leads to an even wider range of Mn–O bond distances than is observed in Bi₂NiMnO₆. This may assist in the accommodation of the Bi³⁺ displacements under ambient pressure synthesis conditions of Bi₂Mn_{4/3}Ni_{2/3}O₆.

B Site Cation Order. The local short-range order of the B site cations was investigated by nearest neighbor calculations of $n(r)$ (eq 1), defined³⁴ as the mean number of atoms surrounding a central atom. It has been used to find A site cation ordering in Ca_xSr_{1-x}TiO₃.³²

$$n_{ij}(r) = \int_{r_2}^{r_1} 4\pi r^2 c_j \rho_0 g_{ij}(r) dr \quad (1)$$

where ρ_0 is the average number density of the material, c_j is the proportion at atom j in the material, and g_{ij} is the partial distribution function for atoms i and j . $n(r)$ was calculated directly from the partial pair distribution function $g_{B-B}(r)$ where the average numbers of neighbors for each pair of B site cations between distances r_1 and r_2 have been extracted (Figure S3). Distributions from the RMC local structure were compared with the results of data-free refinements that displayed completely random distributions. The average number of neighbors differs significantly between the observed and random distributions (Tables 3 and 4) for both RT and HT structures. The most pronounced difference in the RT structure are observed for the first coordination sphere of Ni

cations where the observed $n_{Ni-Ni}(r)$ of 1.64(1) and $n_{Ni-Mn}(r)$ of 4.36(1) are significantly different than for a random distribution (2 and 4, respectively) (Figure 6a,b). The $n(r)$ calculations represent the average results of 20 RMC models, and the standard errors quoted are based on standard deviations of the results for the 20 models. The values for the first and second neighbors calculated for the 20 individual RMC models were essentially the same for each model and thus produce small standard deviation of 0.01, which confirms that this deviation from random cation ordering revealed through RMC modeling is a real result of the data. We therefore assign this observation of a reduction in Ni–Ni nearest neighbor pairs when compared to a random B site distribution to short-range Mn/Ni cation site ordering. Consistent with this reduction in the first nearest neighbor $n_{Ni-Ni}(r)$, the second nearest neighbor $n_{Ni-Ni}(r)$ is significantly higher than random. This decrease of $n_{Ni-Ni}(r)$ in the first shell and increase in the second are consistent with a bias toward rock salt ordering, which is observed in the related stoichiometric high pressure phase Bi₂MnNiO₆.^{35,36} This B site ordering within a representative section of an RMC model is visualized in Figure 7a, where B site cations are colored relative to the numbers of Ni/Mn in the six nearest neighbors, while gray atoms represent the average 4Mn/2Ni ratio. The regions of rock-salt-type ordering are clearly visible in the configuration despite the 2:1 Mn/Ni ratio of BMN being far from the ideal 1:1 ratio required for perfect rock salt ordering. In consequence, there are regions of higher concentrations of Mn cations (blue), which are necessary in order to produce the high concentrations of Ni cations (red) needed to form rock salt ordered regions. The search for short-range ordering past the second nearest neighbor using $n(r)$ calculations is prevented by overlap of atoms between nearest neighbor shells.

The cation ordering motifs within the RT average incommensurate structure was also probed using the same $n(r)$ calculations. The RMC sized models of the incommensurate structure, where B sites were randomly assigned in a manner consistent with the occupational probability from the modulated model, were used for these the $n(r)$ calculations. The $n(r)$ results for this incommensurate model (Table 5 and Figure 6e,f) do not show the rock salt ordering present in the local structure. However, the absence of order in this type of $n(r)$ calculation does not necessarily mean that there is no cation ordering whatsoever; different ordering patterns can still result in the random 4Mn/2Ni nearest neighbor ratio. The RT incommensurate average structure does indeed show nearest neighbor B site ordering; however, $n(r)$ calculations are insensitive to this particular ordering pattern. The nature of the ordering is thus different than found for the RMC local structure. Figure 7b shows the general pattern of B site ordering in the incommensurate approximant supercell (395 Å × 147 Å

Table 3. B Site Nearest Neighbors for the Local Structure Derived from RMC Modeling of the RT Phase of Bi₂Mn_{4/3}Ni_{2/3}O₆^a

B site–B site	$n(r)$ of first shell, 6 neighbors		$n(r)$ of second shell, 12 neighbors		$n(r)$ of third shell, 8 neighbors	
	RMC local structure	disordered	RMC local structure	disordered	RMC local structure	disordered
Mn–Mn	3.82(1)	4.0	8.29(1)	8.0	5.21(2)	5.33
Mn–Ni	2.18(1)	2.0	3.71(1)	4.0	2.79(3)	2.66
Ni–Mn	4.36(1)	4.0	7.41(1)	8.0	5.54(6)	5.33
Ni–Ni	1.64(1)	2.0	4.59(1)	4.0	2.46(7)	2.66

^a $n(r)$ is given for the refined RMC local structure (with standard errors derived from the standard deviation between the 20 different supercell models) and a fully disordered B site distribution.

Table 4. B Site Nearest Neighbors for the Local Structure of the Commensurate (HT) Phase^a

B site–B site	$n(r)$ of first shell, 6 neighbors		$n(r)$ of second shell, 12 neighbors		$n(r)$ of third shell, 8 neighbors	
	RMC local structure	disordered	RMC local structure	disordered	RMC local structure	disordered
Mn–Mn	3.76(2)	4.0	8.25(3)	8.0	5.28(5)	5.33
Mn–Ni	2.24(2)	2.0	3.75(3)	4.0	2.71(7)	2.66
Ni–Mn	4.49(3)	4.0	7.52(4)	8.0	5.41(6)	5.33
Ni–Ni	1.51(3)	2.0	4.48(4)	4.0	2.60(8)	2.66

^aComparison between the refined RMC local structure values (with standard errors) and the disordered distribution shows comparable results to the RT phase, with an observable preference for Ni–Mn near-neighbor clustering.

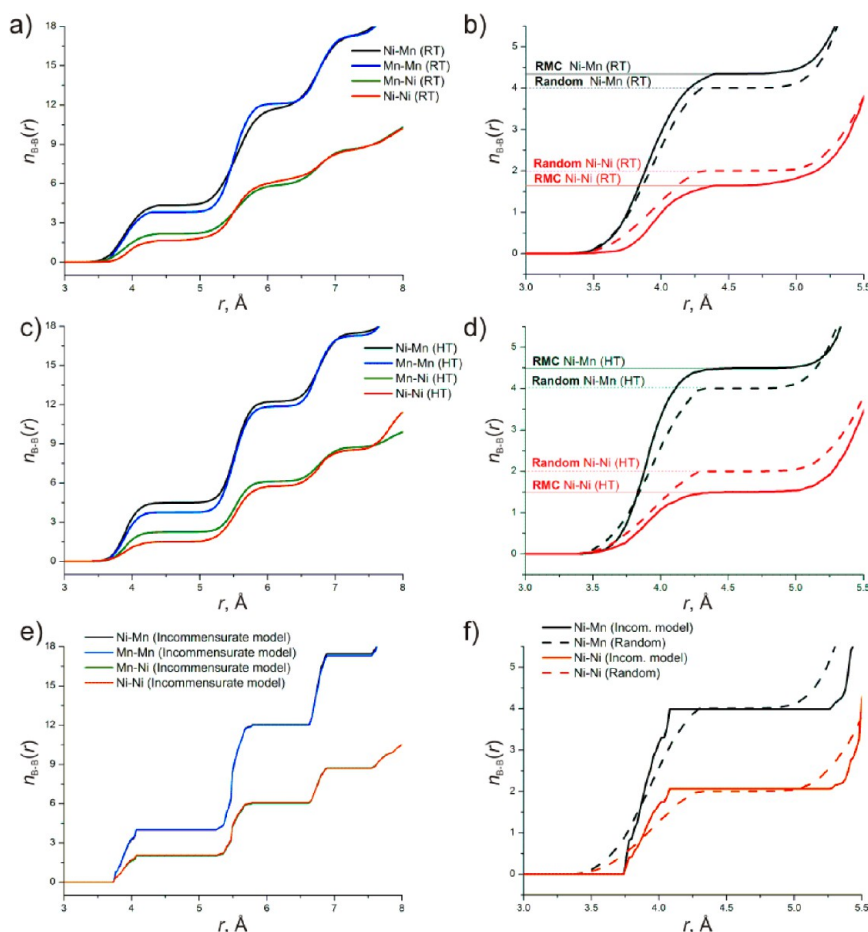


Figure 6. Nearest neighbor functions $n_{B-B}(r)$ (a) at RT and (c) at HT show noticeable differences in the RMC local structure from those compared for a statistically disordered distribution, (b) and (d), respectively. Nearest neighbor functions $n_{B-B}(r)$ from the average incommensurate model (e) indicate comparable results to statistically disordered distribution (f). Results are also presented in Tables 3–5

$\times 5.5 \text{ \AA}$) where polyhedra are colored according to the fractional occupancy of the B site. Instead of the rock-salt-type order observed in the RMC local structure, the incommensurate structure displays a more complex Mn/Ni clustering, forming 2×2 columns of nickel rich and manganese rich octahedral forming a checkerboard pattern. The average structure is refined against modulations of defined periodicity, and the orderings seen in that structure correspond to that periodicity over distances comparable to the wavelength of the modulation. This long-range modulated ordering is not of rock-salt type, being derived from modulation Bragg peaks of the type $hklmn$ ($m, n = \pm 1$), but it is possible that it is an average over ordered and disordered regions and that these disordered regions may include short-range rock-salt ordering. The PDF analysis thus reveals a distinct *short-range* ordering of rock salt

type to which any average structure analysis is necessarily insensitive.

The short-range rock-salt-type cation order observed in the RMC analysis of the incommensurate RT structure persists at HT in the commensurate structure, with $n_{Ni-Ni}(r)$ and $n_{Ni-Mn}(r)$ for the first nearest neighbor of 1.51(3) and 4.49(3) (Figure 6c,d). This result emphasizes how the single B site in the long-range average HT structure fails to fully describe the true local structure of HT BMN and confirms the information extracted from the more complex RT structure by RMC analysis. Here the RMC local structure contains new information on the B site ordering, which is entirely absent from both the long-range incommensurate (RT) and commensurate (HT) structures.

Polar Local Displacements of Bi^{3+} . By collapsing RMC models onto the original orthorhombic cells in both the RT

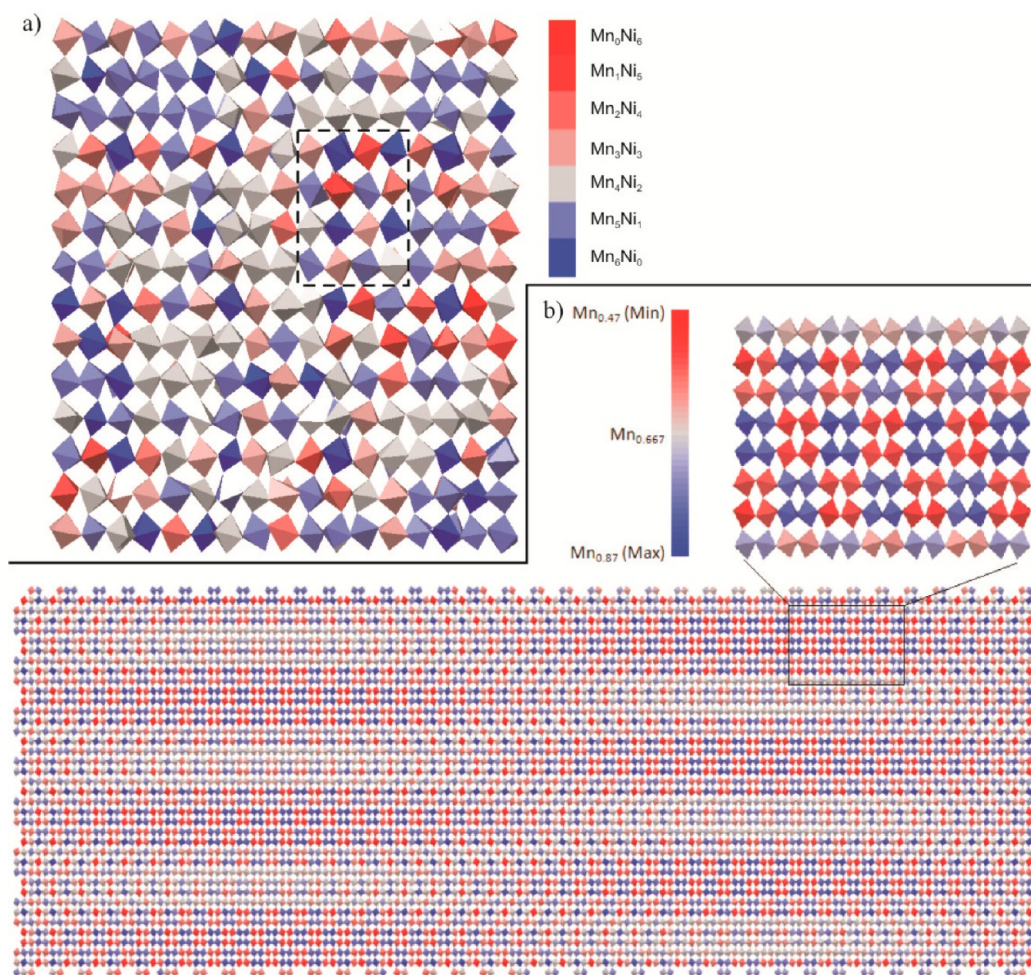


Figure 7. (a) B site ordering in a representative portion of an RMC model displaying a rock-salt-type ordering pattern (outlined in a dotted black line). B site cations are colored according to the number of the six nearest neighbors of different atom types, with blue and red atoms corresponding to high and low numbers of Mn nearest neighbors, respectively, and gray representing the average value of 4Mn (in accordance with the chemical composition $\text{Bi}_2\text{Mn}_{4/3}\text{Ni}_{2/3}\text{O}_6$). (b) Approximant cell of incommensurate structure ($71\sqrt{2}a_p \times 38a_p \times \sqrt{2}a_p$), viewed down along the nonmodulated $\langle 110 \rangle_p$ axis. B site cations are colored according to fractional occupancy, with blue and red atoms corresponding to high and low occupancy probability of Mn cations and gray representing the compositional average $\text{Mn}_{0.667}$. The cell has sufficient size to provide a view of the range of environments and demonstrate the clustering of Mn/Ni cations due to occupational modulations. The enlarged section shows the Mn/Ni clustering.

Table 5. B Site Nearest Neighbors for the Average Incommensurate (RT) Model^a

B site–B site	$n(r)$ of first shell, 6 neighbors		$n(r)$ of second shell, 12 neighbors		$n(r)$ of third shell, 8 neighbors	
	average incommensurate model	disordered	average incommensurate model	disordered	average incommensurate model	disordered
Mn–Mn	4.03(3)	4.0	8.05(6)	8.0	5.35(4)	5.33
Mn–Ni	2.02(3)	2.0	4.03(3)	4.0	2.70(2)	2.66
Ni–Mn	4.03(6)	4.0	8.08(8)	8.0	5.41(4)	5.33
Ni–Ni	2.02(4)	2.0	4.02(5)	4.0	2.66(4)	2.66

^aComparison between the incommensurate model values (with standard errors) and the disordered distribution shows very comparable results.

and HT structure, details of the atomic displacements can be seen on the local scale. The commensurate HT structure (Figure 8b) contains two clouds of bismuth atoms displaced in opposite directions, which confirms the simple antiferroelectric displacement character of the A site cations in this commensurate structure. The bismuth atoms in the RT structure (Figure 8a) present a more complex structured distribution. This led us to study displacements of the A site cations from the centroids of their 12-coordinating oxides. Given the random nature of a Monte Carlo refinement and the

strong pseudo-tetragonal nature of the starting cell, it is possible for these displacements to refine to either of the available $\langle 110 \rangle_p$ directions. Calculations of the total A site cation displacements (Figure 9a) and those along nonpolar $\langle 110 \rangle_p$ (Figure 9c) show bimodal displacements, characteristic of the antiferroelectric displacements within BMN and a single Gaussian shape along polar $\langle 1\bar{1}0 \rangle_p$ and nonpolar $\langle 001 \rangle_p$ (Figure 9b, d) in both the average incommensurate model and the refined RMC model. The distribution along polar $\langle 1\bar{1}0 \rangle_p$ is represented by single broad Gaussian shape, due to

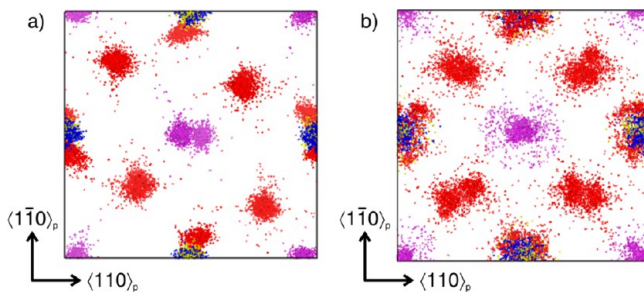


Figure 8. Projection of the atomic positions of $\text{Bi}_2\text{Mn}_{4/3}\text{Ni}_{2/3}\text{O}_6$ from the RMC supercell into the original unit cell viewed along $\langle 001 \rangle_p$ for the local structure at (a) RT and (b) HT. Atoms are colored as follows: Bi purple, Mn blue, Ni yellow, and O red.

the presence of both positive and negative displacements of Bi^{3+} cations. The different magnitudes of displacement in opposite directions produce local polarity along $\langle 1\bar{1}0 \rangle_p$, which cancels out over long range to produce antiferroelectric displacements in the incommensurate average structure. The Bi displacement distribution for the RMC model appears symmetric, indicating that the RMC supercell has minimal net polarity, as observed for the approximant incommensurate supercell. The RMC model gives a broader atomic displacement distribution than observed for the average incommensurate model; this is consistent with the similarly broader RMC model $g_{\text{Bi-O}}(r)$ distribution and is a consequence of thermal motion in the local structure.

The absence of a net Bi displacement, and therefore polarity, within the RMC supercell led us to investigate local correlations between the Bi displacements. Correlations between atomic displacements can be identified through evaluation of the displacement correlation function (DCF), which is defined between two species according to eq 2:

$$\eta(r) = \frac{1}{Nr^2} \sum \mathbf{u}_i \cdot \mathbf{u}_j \quad (2)$$

where the \mathbf{u}_i and \mathbf{u}_j vectors define displacement of atoms i and j , respectively, while N and r correspond to number of atoms and their separation, respectively. The displacement of each Bi, \mathbf{u} , was calculated from the centroid of their neighboring 12 oxygen atoms, and DCF was summed over the volume of the RMC supercell. To eliminate the inherent contribution coming from the symmetry of the crystallographic average structure, the DCF of a completely randomized RMC configuration was calculated and subtracted from the calculated DCF, as previously applied for the ferroelectric material $\text{Bi-Ti}_{3/8}\text{Fe}_{2/8}\text{Mg}_{3/8}\text{O}_3$.²⁵ Randomized RMC configurations were created by statistically swapping centroid displacements between the atoms. The difference between the RMC configuration and the randomized configuration should provide the real correlations beyond those arising from the average structure in the material. The DCF was calculated at the interatomic separation r between pairs of atoms and can be resolved into distinct planes within the structure and along the polar $\langle 1\bar{1}0 \rangle_p$ and the two nonpolar $\langle 001 \rangle_p$ and $\langle 110 \rangle_p$ directions. A positive value means that the displacements of Bi atoms separated by distance r are ferroelectrically correlated, whereas negative peaks indicate antiferroelectric correlations.

The most intense peaks in the DCF of the RMC model (Figure 10a) are along $\langle 110 \rangle_p$ with a pattern of both positive and negative peaks. This is an effect of antiparallel displacement shifts between Bi^{3+} cations along this direction (Figure 10b). These antiferroelectric correlations are also observed in the average incommensurate model (Figure 10c). These dominant peaks along $\langle 110 \rangle_p$ are very comparable to those found in $\eta_{\text{Pb-Pb}}(r)$ calculated for $\text{PbZrO}_3(\text{PZ})$ (Figure 11a) where Pb^{2+} atoms describe a well-known antiferroelectric pattern of displacements along $\langle 110 \rangle_p$ (Figure 11b), demonstrating that the Bi^{3+} cation correlations in the RMC and average

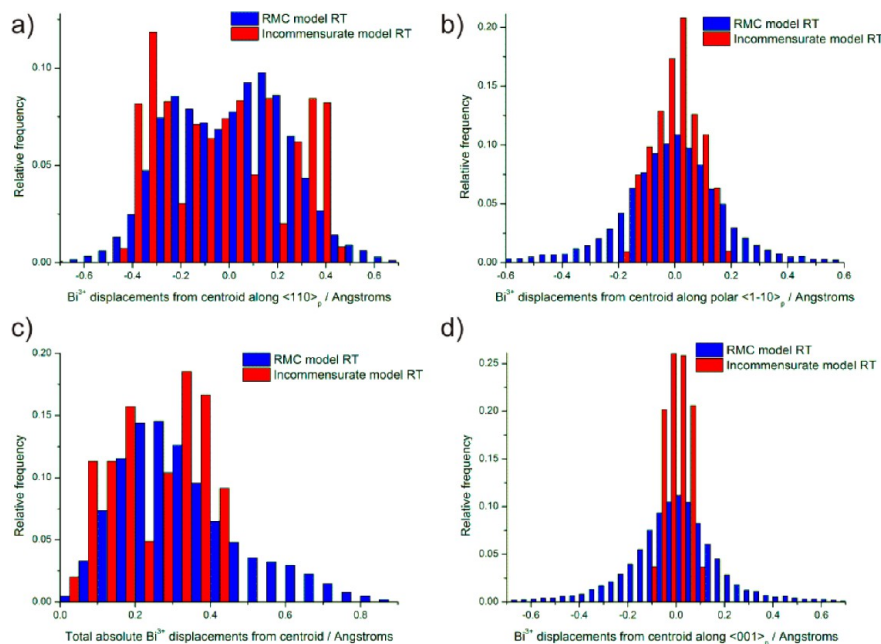


Figure 9. (a) Comparison of total absolute displacements of the Bi cations from the centroid of the coordinating oxygens between the RMC local structure and the average incommensurate model. Comparison of the distribution of Bi displacements from the oxygen centroid along (b) $\langle 1\bar{1}0 \rangle_p$, (c) $\langle 001 \rangle_p$, and (d) $\langle 110 \rangle_p$.

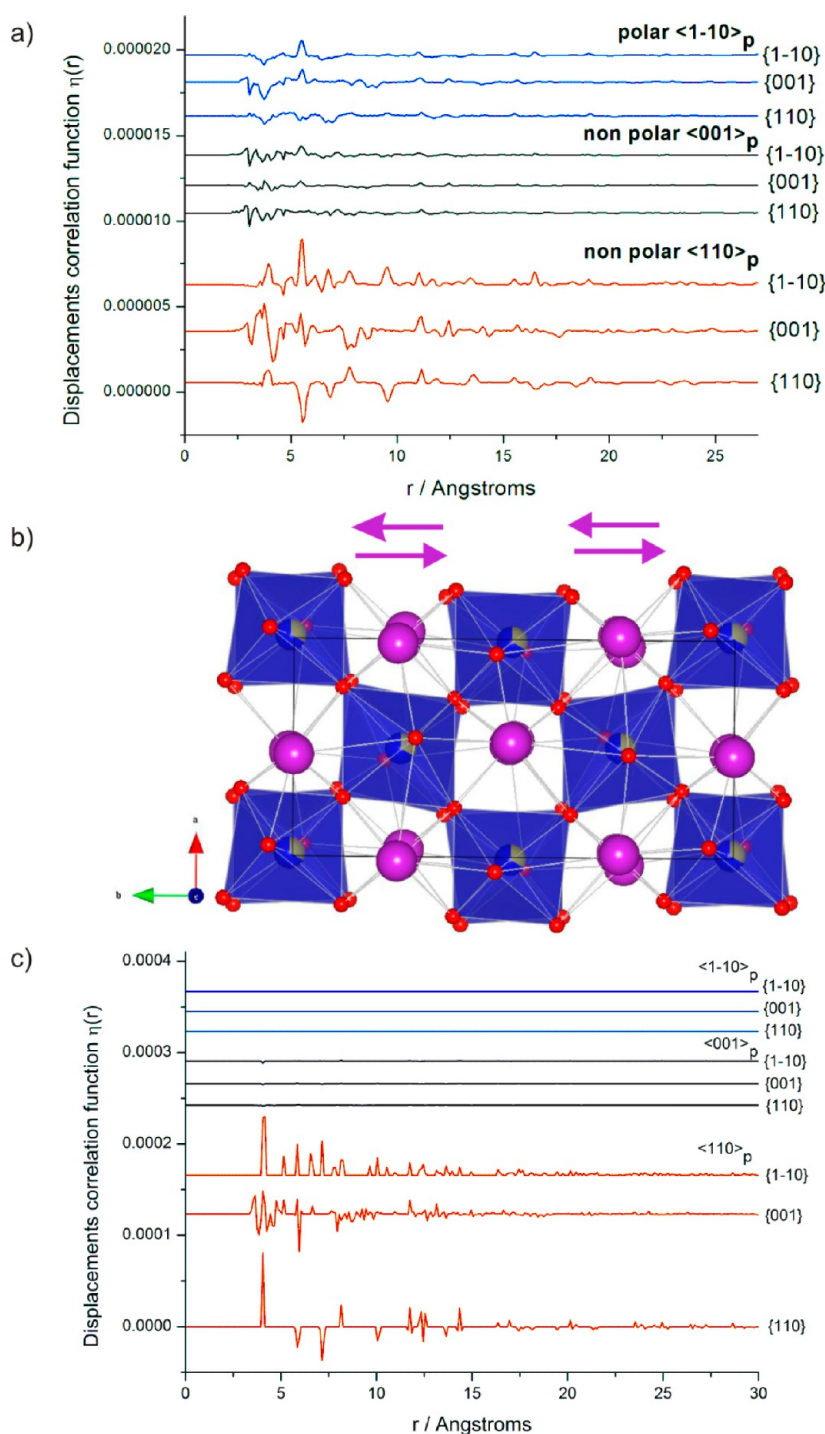


Figure 10. (a) Differential DCF for Bi–Bi in the RMC local structure model showing antiparallel displacement along $\langle 110 \rangle_p$, as illustrated in (b). (c) Differential DCF for Bi–Bi for the average incommensurate model, demonstrating general agreement between RMC and incommensurate models.

incommensurate model of BMN have the same pattern as in antiferroelectric PZ along $\langle 110 \rangle_p$. This feature is retained, with broadening, in the commensurate HT structure (Figure S4).

The $\eta_{\text{Bi-Bi}}(r)$ for the RT RMC model (Figure 10a) and the average incommensurate model (Figure 10c) both demonstrate a pattern of small negative and positive peaks along $\langle 110 \rangle_p$, indicating weak antiferroelectric correlations that appear because the different direction of displacement for the neighboring atoms is the dominant effect in the DCF. Thus, instead of observing polar nanoregions (with ferroelectric correlations in the DCF), we observe antiferroelectric

correlations consistent with the long-range modulated average structure. These correlations along $\langle 1\bar{1}0 \rangle_p$ and $\langle 001 \rangle_p$ almost disappear in the HT phase.

We hypothesize that the polar correlations do exist at RT along $\langle 110 \rangle_p$ within a larger volume rather than having strong correlations between single pairs of atoms as probed by the DCF calculations. In order to test this hypothesis, we looked at the sum of Bi displacements, relative to the center of charge of the 12 nearest neighbor oxygens, within a volume. The sum of Bi^{3+} displacements was calculated by taking the B site cations as the origin and summing the displacement of every Bi^{3+} within a

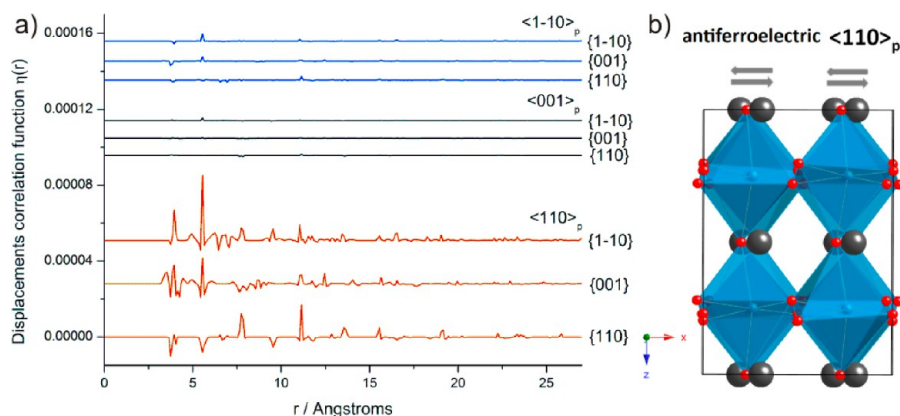


Figure 11. (a) Differential DCF for Pb–Pb in PZ with antiparallel displacement along $\langle 110 \rangle_p$, as illustrated in (b).

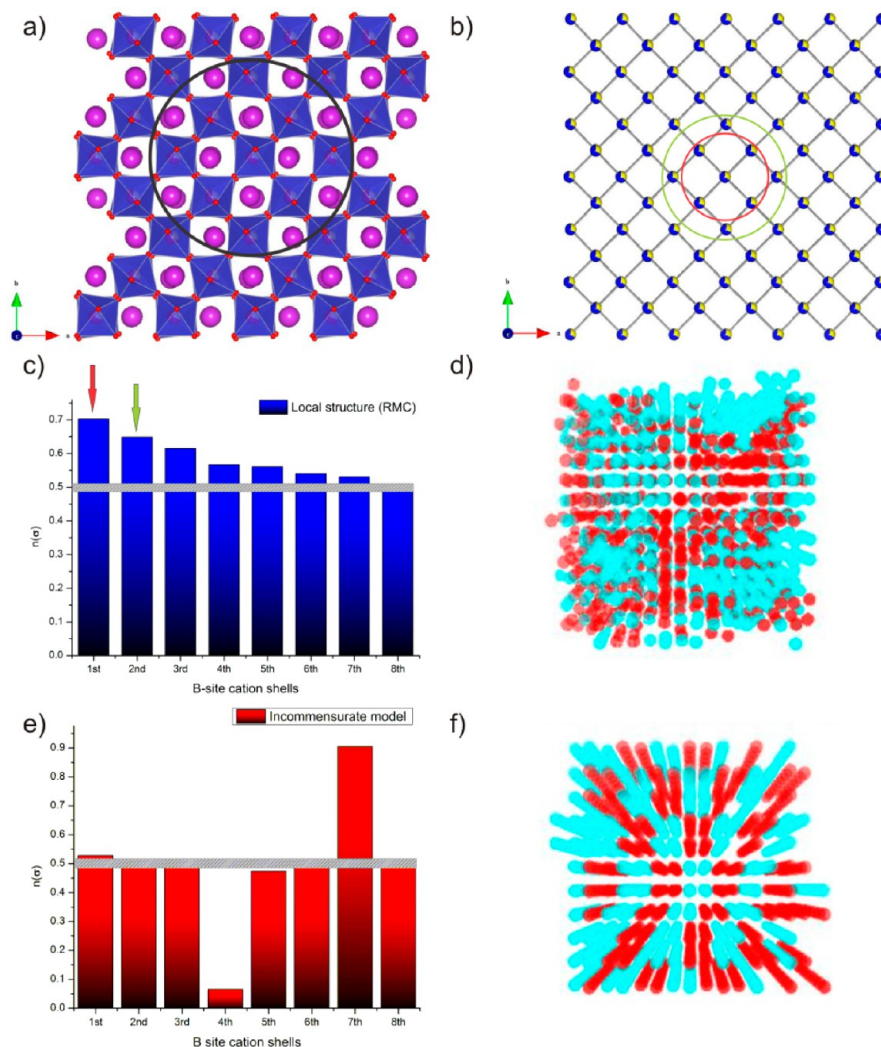


Figure 12. Calculation of Bi^{3+} cation summed displacements. (a) Bi^{3+} cation displacements are summed within a sphere of radius of 7.5 Å, with B site cations as the origin. (b) Illustration of B site atomic shells used to sum volumes of Bi^{3+} displacements, showing first (red circle) and second (green circle) shells. The ratio of Bi^{3+} cations displaced in the same direction along $\langle 1\bar{1}0 \rangle_p$, summed over all bismuth atoms for (c) the RMC local structure model at RT and (e) the incommensurate model at RT. A random distribution of Bi^{3+} displacements is presented as a gray error bar. Supercells with B site cations colored representing positive (red) and negative (blue) sum of neighboring Bi cations along $\langle 1\bar{1}0 \rangle_p$ for (d) the RMC local structure model at RT and (f) the incommensurate model at RT. The RMC model (d) shows clusters of oppositely displaced groups of atoms, clearly indicating local ferroelectric correlations between the Bi atoms, whereas the incommensurate model (f) shows sinusoidal behavior of displaced Bi atoms resulting from the incommensurate character of this model.

given radius, r . An r value of 7.5 Å and the B site as the origin were selected in order to return 16 Bi^{3+} cations (an even

number to ensure that net polarity is not inevitable) and contain a volume approximately equivalent to that of the polar

commensurate subcell; as the Bi displacements are relative to the center of charge, this measure is independent of the B site displacements. The sum of the Bi^{3+} displacements along the polar $\langle 1\bar{1}0 \rangle_p$ direction was calculated, and the ratio of Bi^{3+} cations displaced in the same direction over all bismuth atoms was evaluated for each atomic shell (Figure 12a,b). Thus, the ratio expressed in eq 3 with values above 0.5 gives information about atomic correlations.

$$s(\sigma) = \frac{\sum s(+)}{\sum (s(+) + s(-))} \quad (3)$$

where σ represents an atomic shell, $\sum s(+)$ corresponds to sum of Bi^{3+} cations displaced in the same direction along $\langle 1\bar{1}0 \rangle_p$, and $\sum (s(+) + s(-))$ defines the overall sum of Bi^{3+} cations displaced in opposite directions along $\langle 1\bar{1}0 \rangle_p$.

These calculations showed that local correlations of Bi^{3+} cation displacements do indeed exist within a distance of approximately 12 Å (Figure 12c) when compared to the randomly distributed Bi^{3+} cations observed in the supercells generated from data-free refinements (presented as an error bar). There is a strong correlation within the first atomic shell with an $s(1)$ ratio of 0.71, which gradually decreases toward the random value of 0.5, reaching a value of 0.52 (i.e., no significant correlation) for $s(8)$. Figure 12d shows an RT RMC supercell with the positive (red) and negative (blue) atoms representing the sum of Bi displacements in opposite directions along $\langle 1\bar{1}0 \rangle_p$; groups of atoms gathering in clusters are clearly present indicating the local correlations between Bi atom displacements. These clusters with oppositely displaced atoms which cancel out to no net polarity within the RMC supercell (as evidenced by the symmetric distribution of the Bi displacement distribution; cf. Figure 9b) are similar to the polar regions in the long-range approximant supercell of the incommensurate structure which cancel each other to produce long-range average antiferroelectric displacements.

The size of the BMN polar domains is not easy to define from the long-range average structure. Equivalent $s(n)$ calculations for Bi displacements in the incommensurate structure result in large minima and maxima appearing repeatedly at fixed distances (Figure 12e) and a checkerboard pattern of polar regions along the modulated directions that form infinite chains along the nonmodulated direction (Figure 12f). What we can say from long-range Bragg diffraction is that the polar regions are probably at least the size of the polar approximant commensurate subcell ($P2_1mn$, $2\sqrt{2}a_p \times 4a_p \times \sqrt{2}a_p$, $a = 11.1496$ Å, $b = 15.5302$ Å, and $c = 5.5092$ Å), given this reasonably good fit of this polar structure to the Bragg data, and the absence of polarity in an approximate incommensurate supercell ($71\sqrt{2}a_p \times 38a_p \times \sqrt{2}a_p$) demonstrates that polar regions are at most half this larger size.¹⁶ By calculating $s(n)$ for Bi in RT RMC models of the local structure BMN, we are able for the first time to quantify the size of the polar domains as existing within a domain of ~ 12 Å, in reasonable agreement with the long axis dimensions of the polar approximant commensurate subcell. As opposed to the average commensurate subcell, which is entirely polar, and the approximate incommensurate supercell, where polarity is modulated in two dimensions, the local structure shows how Bi^{3+} displacements are correlated in three dimensions in real space.

Local correlations with dimensions of up to 12 Å persist in the HT phase, where the sum of Bi atoms displaced in the same direction along $\langle 1\bar{1}0 \rangle_p$ also creates polar clusters (Figure 13).

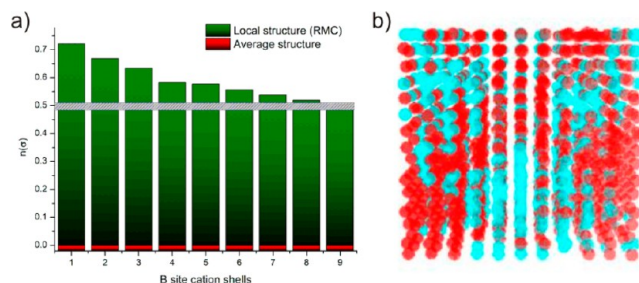


Figure 13. (a) Comparison of the ratio of Bi cations displaced in the same direction along $\langle 1\bar{1}0 \rangle_p$ over all bismuth atoms between the RMC local structure (green) and average commensurate structure (red) at HT. The random distribution is presented as an error bar (gray). (b) RMC supercell with B site cations colored according to positive (red) or negative (blue) sum of neighboring Bi cation displacements along $\langle 1\bar{1}0 \rangle_p$. Clusters of Bi cations displaced in the same direction persist in the HT phase.

This is unexpected as the average structure at HT has only antiferroelectric correlations. The displacements of Bi^{3+} cations in the average HT commensurate structure completely cancel out (red columns in Figure 13a), which is in agreement with this antiferroelectric displacement of Bi atoms. The observation of local ferroelectric correlations in the HT phase means that the local displacements of Bi^{3+} cations giving rise to short-range polar regions still exist above the phase transition from the RT incommensurate structure to the HT commensurate structure, despite there being no signs of this polar nature in the long-range average crystallographic structure, suggesting that these correlations are now dynamic. These locally correlated polar regions would be expected below the Burns temperature of a relaxor or conventional ferroelectric, consistent with the measurement being performed only about 100 K above the structural transition. The resulting deviation from Curie–Weiss behavior is unfortunately not observable by direct measurement, as the material is too lossy in this temperature range because of the mixed manganese valence.

CONCLUSIONS

The availability of local structure information changes the understanding of the chemical stability and physical properties of incommensurate $\text{Bi}_2\text{Mn}_{4/3}\text{Ni}_{2/3}\text{O}_6$ (BMN) in several significant respects. The B site environment at RT is significantly different in the RMC local structure and average incommensurate model. The application of BVS and interatomic potential constraints in the RMC modeling allowed us to differentiate between Ni and Mn on the B site, which share the same site in the incommensurate average structure. Analysis of the Mn–O environment reveals a 2:2:2 J–T distortion for the Mn^{3+} cations, similar to that observed in $\text{Bi}_{1-x}\text{Ca}_x\text{MnO}_3$. The presence of different Mn charge states, and the potential for J–T distortions, gives rise to a wide range of Mn–O bond lengths that, together with the distinction between Bi–Mn and Bi–Ni distances seen in the local structure, will enable BMN to accommodate the off-center displacement of the Bi^{3+} cations required to explain its unusual stability to ambient pressure synthesis.

Inspection of partial pair distribution functions for both the RMC local structure and average incommensurate models showed three preferred Bi–O bond distances at similar Bi–O distances that were consistent with antiparallel displacement of Bi cations along $\langle 110 \rangle_p$. For the incommensurate average

structure, $g_{\text{Bi-O}}(r)$ shows two different discontinuous distributions, one of which contained a short Bi–O bond resulting from maxima in the applied displacive modulations. The local analysis does not include such features and thus produces a chemically preferable description of the bonding at Bi^{3+} .

At RT, both incommensurate and RMC models show B site ordering; however, the nature of the ordering is quite different. The RMC local structure reveals rock-salt-type nearest neighbor ordering, which is adopted by the related stoichiometric high pressure phase $\text{Bi}_2\text{MnNiO}_6$, with the additional disorder necessitated by the 2:1 Mn/Ni ratio of BMN. The incommensurate average structure is insensitive to this and produces Mn/Ni clustering on the B site corresponding to the periodicity of the modulation. There are thus two ordering motifs present over different length scales, emphasizing that despite the perceived diversity of local atomic environments present within an incommensurate structure description, these atomic displacements and site orderings are a result of long-range modulations. As such, they may not reflect the true local nature of atomic displacements present within the structure and cannot contain displacements or orderings not described by the modulation waves used, e.g., the simple rock-salt-like order on the B site. The same local rock salt ordering is observed for the HT phase, where the average *Pcnm* commensurate structure displays no ordering whatsoever, although the peaks due to the long-range modulated cation order are still visible in the neutron diffraction data.¹⁶

The local structure analysis thus identifies three important chemical features for the stability of the material, namely, the short-range B site ordering, the distribution of Bi–O distances, and the wide range of B–O distances accommodated by different Mn charge states and a J–T distortion. The coexistence of two distinct B site ordering patterns over different length scales may play a role in stabilizing this Bi^{3+} A site material. The local structure of $\text{BiTi}_{3/8}\text{Fe}_{2/8}\text{Mg}_{3/8}\text{O}_3$ reveals flexible coordination behavior of Ti^{4+} on the B site, which may play a similar role to the three Mn–O distances in the preferred J–T distortion at Mn^{3+} here, but there is no B site ordering over any length scale in this commensurate system. The local structures of these two examples thus suggest that a range of chemical strategies may be deployed to stabilize Bi^{3+} A site perovskites.

Calculation of Bi^{3+} displacements showed a bimodal distribution along the nonpolar $\langle 110 \rangle_p$ at RT in both the incommensurate average structure model and the RMC local structure, accounting for the antiferroelectric displacement behavior of BMN. The Bi–Bi displacement correlation function along the same direction shows similar peaks in both RMC and average incommensurate models that are consistent with the antiferroelectric behavior of PbZrO_3 ; this feature is preserved in the local structure of the HT phase. As recent work suggests that PZ itself adopts this structure because of a “narrowly missed” ferroelectric instability,³⁷ this observation is consistent with the presence of polar local features in BMN (i.e., that BMN may also be close to global ferroelectric instability as observed in high pressure $\text{Bi}_2\text{MnNiO}_6$) and indicates that PZ-like systems may be accessible in Bi-based perovskites.

Bi^{3+} displacements along the polar $\langle 1\bar{1}0 \rangle_p$ showed a single Gaussian distribution for both the incommensurate average structure model and the RMC local structure model, indicating that overall the models are nonpolar. Attempts to uncover local ferroelectric polar Bi–Bi displacements by calculation of the displacement correlation function instead revealed antiferro-

electric correlations that would appear to negate the presence of polar regions. Instead, polarity is produced on the local scale by different magnitudes of positive and negative displacements along $\langle 1\bar{1}0 \rangle_p$, which generate a net polarity despite the dominant displacement correlation between neighboring Bi atoms being antiferroelectric. The true nature of the polar behavior of BMN was revealed by calculating the sum of Bi displacements within a volume, which showed that ferroelectric correlations along $\langle 1\bar{1}0 \rangle_p$ within the RMC local structure at RT give rise to polar clusters with a size of up to 12 Å. This local structure analysis allowed the size of the polar domains, which is elusive from long-range average structure treatments, to be quantified for the first time. These local polar domains are preserved at HT, where the long-range average structure shows no signs of this underlying polar nature.

Recognizing the length-scale of the probe used for structural characterization is very important for the interpretation of the results. Average structures derived from Bragg diffraction data are an invaluable tool for structure characterization on the long length scale, but frequently important structural characteristics such as short-range order or cooperative displacements can be missed entirely. Here total scattering analysis has provided new insights into the incommensurate structure of the atmospheric pressure synthesized Bi perovskite $\text{Bi}_2\text{Mn}_{4/3}\text{Ni}_{2/3}\text{O}_6$, revealing features of direct relevance for its unusual stability and explaining the structural and functional relationship to better-studied lead-based systems.

■ ASSOCIATED CONTENT

Supporting Information

Correlations between Bi–B and B–B displacements, displacement of B site cations from the center of their oxygen environment, comparison of Bi–B site bond distances, bond angle distributions, the partial pair correlation functions, and differential displacement correlation functions (PDF). This material is available free of charge via the Internet at <http://pubs.acs.org>.

■ AUTHOR INFORMATION

Corresponding Author

*E-mail, J.B.Claridge@liverpool.ac.uk.

Author Contributions

The manuscript was written through contributions of all authors. All authors have given approval to the final version of the manuscript.

Notes

The authors declare no competing financial interest.

■ ACKNOWLEDGMENTS

We acknowledge Prof. Alex C. Hannon for assistance with correction of total scattering data and Dr. Andrew L. Goodwin for help in determining displacement correlation functions. We thank the STFC for access to the ISIS Facility. This work was supported by the European Research Council under the seventh Framework Program (FP7) (ERC Grant agreement 227987 RLUCIM). We thank the Engineering and Physical Sciences Research Council for access to ISIS and for a studentship for R.J.S.

■ REFERENCES

- (1) Bosak, A.; Chernyshov, D.; Vakhruшев, S. *J. Appl. Crystallogr.* **2012**, *45*, 1309.

- (2) Haertling, G. H. *J. Am. Ceram. Soc.* **1999**, *82*, 797.
- (3) Burkovsky, R. G.; Bronwald, Y. A.; Filimonov, A. V.; Rudskoy, A. I.; Chernyshov, D.; Bosak, A.; Hlinka, J.; Long, X.; Ye, Z. G.; Vakhrushev, S. B. *Phys. Rev. Lett.* **2012**, *109*, No. 097603.
- (4) Catalan, G.; Scott, J. F. *Adv. Mater.* **2009**, *21*, 2463.
- (5) Lebeugle, D.; Colson, D.; Forget, A.; Viret, M.; Bataille, A. M.; Gukasov, A. *Phys. Rev. Lett.* **2008**, *100*, 227602.
- (6) Ishiwata, S.; Azuma, M.; Takano, M.; Nishibori, E.; Takata, M.; Sakata, M.; Kato, K. *J. Mater. Chem.* **2002**, *12*, 3733.
- (7) Inaguma, Y.; Katsumata, T. *Ferroelectrics* **2003**, *286*, 833.
- (8) Inaguma, Y.; Miyaguchi, A.; Katsumata, T. In *Solid-State Chemistry of Inorganic Materials IV*; Alario-Franco, M. A., Greenblatt, M., Rohrer, G., Whittingham, M. S., Eds.; Materials Research Society: Warrendale, PA, 2003; Vol. 755, p 471.
- (9) Suchomel, M. R.; Thomas, C. I.; Allix, M.; Rosseinsky, M. J.; Fogg, A. M.; Thomas, M. F. *Appl. Phys. Lett.* **2007**, *90*, No. 112909.
- (10) Kimura, T.; Kawamoto, S.; Yamada, I.; Azuma, M.; Takano, M.; Tokura, Y. *Phys. Rev. B* **2003**, *67*, No. 180401(R).
- (11) Azuma, M.; Takata, K.; Saito, T.; Ishiwata, S.; Shimakawa, Y.; Takano, M. *J. Am. Chem. Soc.* **2005**, *127*, 8889.
- (12) Carlsson, S. J. E.; Azuma, M.; Shimakawa, Y.; Takano, M.; Hewat, A.; Attfield, J. P. *J. Solid State Chem.* **2008**, *181*, 611.
- (13) Hughes, H.; Allix, M. M. B.; Bridges, C. A.; Claridge, J. B.; Kuang, X. J.; Niu, H. J.; Taylor, S.; Song, W. H.; Rosseinsky, M. J. *J. Am. Chem. Soc.* **2005**, *127*, 13790.
- (14) Bridges, C. A.; Allix, M.; Suchomel, M. R.; Kuang, X. J.; Sterianou, I.; Sinclair, D. C.; Rosseinsky, M. J. *Angew. Chem., Int. Ed.* **2007**, *46*, 8785.
- (15) Dolgos, M.; Adem, U.; Wan, X.; Xu, Z.; Bell, A. J.; Comyn, T. P.; Stevenson, T.; Bennett, J.; Claridge, J. B.; Rosseinsky, M. J. *Chem. Sci.* **2012**, *3*, 1426.
- (16) Claridge, J. B.; Hughes, H.; Bridges, C. A.; Allix, M.; Suchomel, M. R.; Niu, H.; Kuang, X.; Rosseinsky, M. J.; Bellido, N.; Grebille, D.; Perez, O.; Simon, C.; Pelloquin, D.; Blundell, S. J.; Lancaster, T.; Baker, P. J.; Pratt, F. L.; Halasyamani, P. S. *J. Am. Chem. Soc.* **2009**, *131*, 14000.
- (17) Egami, T.; Billinge, S. J. L. *Underneath the Bragg Peaks: Structural Analysis of Complex Materials*; Pergamon: Amsterdam, 2003.
- (18) Egami, T. In *Annual Review of Materials Research*; Annual Reviews: Palo Alto, CA, 2007; Vol. 37, p 297.
- (19) Teslic, S.; Egami, T.; Viehland, D. *J. Phys. Chem. Solids* **1996**, *57*, 1537.
- (20) Jeong, I. K.; Lee, J. K. *Appl. Phys. Lett.* **2006**, *88*, 262905.
- (21) Norberg, S. T.; Hull, S.; Mathieu, R.; Eriksson, S. G. *Chem. Commun.* **2010**, *46*, 1455.
- (22) Jeong, I.; Park, C. Y.; Kim, D. J.; Kim, S. H.; Moon, B. K.; Kim, W.; Ahn, C. W. Z. *Kristallogr.* **2011**, *226*, 150.
- (23) Keeble, D. S.; Barney, E. R.; Keen, D. A.; Tucker, M. G.; Kreisel, J.; Thomas, P. A. *Adv. Funct. Mater.* **2013**, *23*, 185.
- (24) Kodama, K.; Iikubo, S.; Shamoto, S. I.; Belik, A. A.; Takayama-Muromachi, E. *J. Phys. Soc. Jpn.* **2007**, *76*, 124605.
- (25) Chong, S. Y.; Szczecinski, R. J.; Bridges, C. A.; Tucker, M. G.; Claridge, J. B.; Rosseinsky, M. J. *J. Am. Chem. Soc.* **2012**, *134*, 5836.
- (26) Kim, H.; Malliakas, C.; Tomic, A.; Tessmer, S.; Kanatzidis, M.; Billinge, S. *Phys. Rev. Lett.* **2006**, *96*, 226401.
- (27) Hannon, A. C. *Nucl. Instrum. Methods Phys. Res., Sect. A* **2005**, *551*, 88.
- (28) Petríček, V.; Dušek, M.; Palatinus, L. *Jana2006*. The crystallographic computing system; Institute of Physics: Czech Republic, 2006.
- (29) Brese, N. E.; O'Keeffe, M. *Acta Crystallogr. Sect. B: Struct. Sci.* **1991**, *47*, 192.
- (30) Tucker, M. G.; Keen, D. A.; Dove, M. T.; Goodwin, A. L.; Hui, Q. *J. Phys.: Condens. Matter* **2007**, *19*, 335218.
- (31) Billinge, S. J. L.; Proffen, T.; Petkov, V.; Sarrao, J. L.; Kycia, S. *Phys. Rev. B* **2000**, *62*, 1203.
- (32) Hui, Q.; Dove, M. T.; Tucker, M. G.; Redfern, S. A. T.; Keen, D. A. *J. Phys.: Condens. Matter* **2007**, *19*, 335214.
- (33) Goodwin, A. L.; Redfern, S. A. T.; Dove, M. T.; Keen, D. A.; Tucker, M. G. *Phys. Rev. B* **2007**, *76*, No. 174114.
- (34) Keen, D. A. *J. Appl. Crystallogr.* **2001**, *34*, 172.
- (35) Kanamori, J. *J. Phys. Chem. Solids* **1959**, *10*, 87.
- (36) Goodenough, J. B. *Phys. Rev.* **1955**, *100*, 564.
- (37) Tagantsev, A. K.; Vaideeswaran, K.; Vakhrushev, S. B.; Filimonov, A. V.; Burkovsky, R. G.; Shaganov, A.; Andronikova, D.; Rudskoy, A. I.; Baron, A. Q.; Uchiyama, H.; Chernyshov, D.; Bosak, A.; Ujma, Z.; Roleder, K.; Majchrowski, A.; Ko, J. H.; Setter, N. *Nat. Commun.* **2013**, *4*, 2229.